Parity nonconservation in atomic thallium

Persis S. Drell* and Eugene D. Commins
Physics Department, University of California, Berkeley, California 94720
and Materials and Molecular Research Division, Lawrence Berkeley Laboratory,
University of California, Berkeley, California 94720
(Received 25 February 1985)

We present a detailed description of new observations of parity nonconservation in the $6^2P_{1/2}\rightarrow 7^2P_{1/2}$ transition (293 nm) in atomic $^{205}_{81}$Tl. Linearly polarized 293-nm photons, polarization $\hat{\boldsymbol{\varepsilon}}$, are absorbed by $6^2P_{1/2}$ atoms in crossed **E** and **B** fields. The transition probability for each Zeeman component contains a pseudoscalar term, proportional to $\hat{\boldsymbol{\varepsilon}}\cdot\mathbf{B}\hat{\boldsymbol{\varepsilon}}\cdot\mathbf{E}\times\mathbf{B}$, arising from interference between the parity-nonconserving $E1$ amplitude $\mathcal{E}_P$ and the Stark $E1$ amplitude βE. This is detected by observation of fluorescence at 535 nm accompanying the decay $(7^2P_{1/2}\rightarrow)$ $7^2S_{1/2}\rightarrow 6^2P_{3/2}$. Systematic corrections, due to imperfect linear polarization and misaligned **E** and **B** fields, are determined precisely by auxiliary experiments and found to be small. Our final result: $\mathrm{Im}[\mathcal{E}_{P/\beta}]\,|_{\mathrm{expt}}=-(1.73\pm0.26\pm0.07)$ mV/cm, where the first uncertainty is statistical, and the second is systematic, is compared with results of other experiments and with theoretical estimates based on the standard SU(2)×U(1) electroweak model.

I. INTRODUCTION

Atomic parity nonconservation (PNC) arises from the interference between the neutral-weak and electromagnetic interactions coupling valence electron to nucleus. Accurate observations of the phenomenon in an atom with structure simple enough for unambiguous theoretical interpretation provide an important test of our understanding of the electroweak interaction, now best described by the standard SU(2)×U(1) model. In a many-electron atom, the contribution to PNC from the coupling of axial electronic and vector nucleonic neutral-weak currents is overwhelmingly dominant, and it scales approximately as Z^3, where Z is the atomic number.[1] Thus the effect is most readily detected in very heavy atoms.

Observations of PNC have been reported in optical rotation experiments in $_{82}$Pb (Ref. 2) and $_{83}$Bi (Ref. 3). However, these atoms are complex, and interpretations of the results in terms of fundamental electroweak couplings are limited by large uncertainties in atomic theory. The single-valence-electron atoms Cs and Tl are considerably simpler and the theoretical uncertainties correspondingly smaller.[4] Stark interference experiments have been carried out on the $6^2S_{1/2}\rightarrow 7^2S_{1/2}$ transition (539 nm) in $_{55}$Cs by Bouchiat *et al.*,[5] and on the $6P_{1/2}\rightarrow 7P_{1/2}$ transition (293 nm) in $_{81}$Tl in our laboratory (see Fig. 1). In a previous experiment on the latter transition,[6] as well as in the cesium experiments, circularly polarized photons were absorbed by ground-state atoms in the presence of an external electric field. Interference between the electric dipole amplitudes caused by PNC and by Stark effect resulted in a helicity-dependent polarization of the excited state, the detection of which yielded a measure of PNC in each case.

In this paper we present a detailed description of a new Stark-interference experiment on the 293-nm transition in $^{205}_{81}$Tl, which makes use of *linearly* polarized 293-nm photons and crossed electric (**E**) and magnetic (**B**) fields.[7] The new technique yields far more precise results for $_{81}$Tl than the old one, and with much smaller systematic corrections.

A brief summary of the present work has been published separately.[8] Here we give a detailed analysis of transition probabilities, a description of the experimental apparatus and procedure, an analysis of systematic errors and corrections, a summary of results, and a comparison with theory and earlier experimental results.

II. TRANSITION PROBABILITIES

A. Components of the transition amplitude

The transition $6^2P_{1/2}\rightarrow 7^2P_{1/2}$ in Tl is forbidden $M1$ with measured amplitude[9]

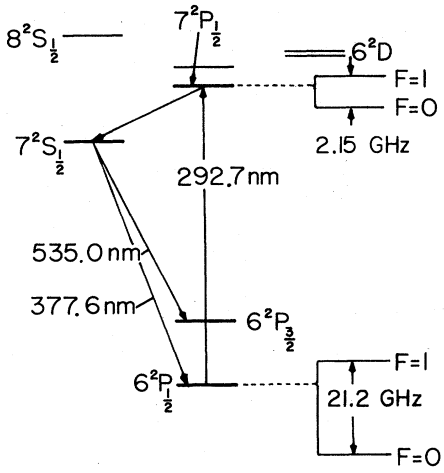

FIG. 1. Low-lying energy levels of Tl (not to scale) showing hyperfine splittings of $6P_{1/2}$ and $7P_{1/2}$ states.

$$M=\langle 7^2P_{1/2}, m_j'=+\tfrac{1}{2} \mid M1 \mid 6^2P_{1/2}, m_j=+\tfrac{1}{2}\rangle$$
$$=(-2.1\pm0.3)\times10^{-5}\mu_0\ , \tag{1}$$

where μ_0 is the electron Bohr magneton: $\mu_0=|e|\hbar/2m_ec$, and $|6^2P_{1/2}\rangle$, $|7^2P_{1/2}\rangle$ are eigenstates of the zero-order electromagnetic Hamiltonian. In the presence of neutral-weak interaction the latter is perturbed by an effective zero-range neutral-weak potential H' that contains both scalar (S) and pseudoscalar (P) parts: $H'=H_S+H_P$. According to the standard model, the dominant contribution to H_P arises from the coupling of axial electronic and vector hadronic neutral-weak currents. In the nonrelativistic limit for nucleon motion, this portion of H_P becomes[1]

$$H_P^{(1)}=\frac{G_F}{2\sqrt{2}m_ec}Q_W\rho(\mathbf{r})\gamma_5\ , \tag{2}$$

where G_F is Fermi's constant, $Q_W=(1-4\sin^2\theta_W)Z-N$, θ_W is Weinberg's angle, N is the number of neutrons in the nucleus, $\rho(\mathbf{r})$ is the nucleon probability density, $\mathbf{r}$ is the valence-electron position, γ_5 is the 4×4 Dirac matrix, and we employ units in which $\hbar=1$.

In the presence of $H_P^{(1)}$, the $6^2P_{1/2}$ and $7^2P_{1/2}$ states are mixed with $^2S_{1/2}$ states. The $6^2P_{1/2}$-$7^2P_{1/2}$ amplitude then contains an $E1$ component

$$\mathcal{E}_P\equiv-\langle\overline{7^2P_{1/2}, m_j'=+\tfrac{1}{2}} \mid E1 \mid \overline{6^2P_{1/2}, m_j=+\tfrac{1}{2}}\rangle \tag{3}$$

where $|\overline{6^2P_{1/2}}\rangle$, $|\overline{7^2P_{1/2}}\rangle$ are eigenstates of the total Hamiltonian including $H_P^{(1)}$. To first order in G_F one has

$$\mathcal{E}_P=-\sum_{nS_{1/2}}\left[\frac{\langle 7P_{1/2},m_j'=+\frac{1}{2} \mid E1 \mid nS\rangle\langle nS \mid H_P^{(1)} \mid 6P_{1/2},m_j=+\frac{1}{2}\rangle}{E_{6P_{1/2}}-E_{nS_{1/2}}}\right.$$
$$\left.+\frac{\langle 7P_{1/2},m_j'=+\frac{1}{2} \mid H_P^{(1)} \mid nS\rangle\langle nS \mid E1 \mid 6P_{1/2},m_j=+\frac{1}{2}\rangle}{E_{7P_{1/2}}-E_{nS_{1/2}}}\right]. \tag{4}$$

Calculations of $\mathcal{E}_P$ have been carried out by a number of authors. Neuffer and Commins[10] employed the one-electron central field approximation (OECF) and a Green-function technique, but ignored many-body effects. They found

$$\mathcal{E}_{P,\text{theor}}^{\text{OECF}}=(+1.93\pm0.40)\times10^{-10}iQ_W\mu_0\ . \tag{5}$$

Das and co-workers[11] used relativistic many-body perturbation theory (RMBPT) and discovered that electron-electron interaction corrections to $\mathcal{E}_P$ are significant. They found

$$\mathcal{E}_{P,\text{theor}}^{\text{RMBPT}}=(+1.51\pm0.07)\times10^{-10}iQ_W\mu_0\ , \tag{6}$$

where in each of (5) and (6) the uncertainties are those estimated by the original authors.

In the presence of an external electric field E the $2P_{1/2}$ states are mixed by the Stark effect with $^2S_{1/2}$ and $^2D_{3/2}$ states. The transition amplitude then acquires a Stark-induced $E1$ component in addition to the $M1$ and $E1_{\text{PNC}}$ portions. For photon linear polarization $\hat{\boldsymbol{\varepsilon}}\perp\mathbf{E}$ the Stark amplitude for $m_j=+\frac{1}{2}\rightarrow m_j=+\frac{1}{2}$ is $i\beta E$. For $\hat{\boldsymbol{\varepsilon}}\parallel\mathbf{E}$, the Stark amplitude for $m_j=+\frac{1}{2}\rightarrow m_j=+\frac{1}{2}$ is αE where α and β are defined to lowest order in terms of dipole radial integrals as

$$\beta=\frac{e^2}{9}\left[\sum_{nS_{1/2}}R_{7P_{1/2},nS_{1/2}}R_{nS_{1/2},6P_{1/2}}\left[\frac{1}{E_{6P_{1/2}}-E_{nS_{1/2}}}-\frac{1}{E_{7P_{1/2}}-E_{nS_{1/2}}}\right]\right.$$
$$\left.+\sum_{nD_{3/2}}R_{7P_{1/2},nD_{3/2}}R_{nD_{3/2},6P_{1/2}}\left[\frac{1}{E_{7P_{1/2}}-E_{nD_{3/2}}}-\frac{1}{E_{6P_{1/2}}-E_{nD_{3/2}}}\right]\right], \tag{7}$$

$$\alpha=\frac{e^2}{9}\left[\sum_{nS_{1/2}}R_{7P_{1/2},nS_{1/2}}R_{nS_{1/2},6P_{1/2}}\left[\frac{1}{E_{7P_{1/2}}-E_{nS_{1/2}}}+\frac{1}{E_{6P_{1/2}}-E_{nS_{1/2}}}\right]\right.$$
$$\left.+2\sum_{nD_{3/2}}R_{7P_{1/2},nD_{3/2}}R_{nD_{3/2},6P_{1/2}}\left[\frac{1}{E_{7P_{1/2}}-E_{nD_{3/2}}}+\frac{1}{E_{6P_{1/2}}-E_{nD_{3/2}}}\right]\right]. \tag{8}$$

According to the calculations of Neuffer and Commins[10]

$$\alpha\,|_{\text{theor}}=(2.05\pm0.30)\times10^{-5}\mu_0\ \text{cm/V}\ , \tag{9}$$

$$\beta\,|_{\text{theor}}=(1.64\pm0.25)\times10^{-5}\mu_0\ \text{cm/V}\ . \tag{10}$$

The ratio β/α is measured to be[9]

$$\beta/\alpha=0.84\ . \tag{11}$$

Until now, neither α nor β is known independently from experiment, although measurements are presently being carried out in our laboratory.

B. Transition probabilities in the ideal case

The coordinate system for the present experiment is shown in Fig. 2. We shall now show that the transition probability for linearly polarized light between any pair of Zeeman sublevels of the $6^2P_{1/2}$ to $7^2P_{1/2}$ states contains a

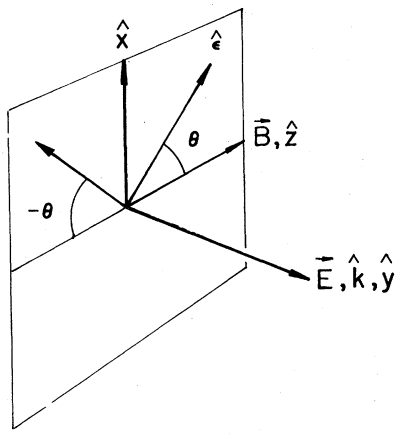

FIG. 2. Experimental coordinate system showing relative orientations of the laser beam ($\hat{\mathbf{k}},\hat{\boldsymbol{\epsilon}}$), the electric field ($\mathbf{E}$), and the magnetic field ($\mathbf{B}$).

term arising from interference between $\mathscr{E}_P$ and βE, that is proportional to $\hat{\boldsymbol{\epsilon}}\cdot\mathbf{B}\hat{\boldsymbol{\epsilon}}\cdot\mathbf{E}\times\mathbf{B}$. Employing $\hat{\boldsymbol{\epsilon}}=\hat{\mathbf{x}}\sin\theta+\hat{\mathbf{z}}\cos\theta$ and $\mathbf{E}=E\hat{\mathbf{y}}$ as in Fig. 2, and using (1) and (3) we have

$$\langle 7^2P_{1/2},F',m_F' \,|\, (E1)_{\text{Stark}}+(E1)_{PNC}+(M1) \,|\, 6^2P_{1/2},F,m_F\rangle$$

$$\langle E1\rangle_{\text{PNC}}= \begin{array}{c} \\ m_j'=\frac{1}{2} \\ m_j'=-\frac{1}{2} \end{array} \begin{array}{c} \begin{array}{cc} m_j=\frac{1}{2} & m_j=-\frac{1}{2} \end{array} \\ \begin{pmatrix} -\mathscr{E}_P\cos\theta & -\mathscr{E}_P\sin\theta \\ -\mathscr{E}_P\sin\theta & +\mathscr{E}_P\cos\theta \end{pmatrix} \end{array}, \tag{12}$$

$$\langle M1\rangle= \begin{array}{c} \\ m_j'=\frac{1}{2} \\ m_j'=-\frac{1}{2} \end{array} \begin{array}{c} \begin{array}{cc} m_j=\frac{1}{2} & m_j=-\frac{1}{2} \end{array} \\ \begin{pmatrix} -M\sin\theta & M\cos\theta \\ M\cos\theta & M\sin\theta \end{pmatrix} \end{array}, \tag{13}$$

and

$$\langle E1\rangle_{\text{Stark}}= \begin{array}{c} \\ m_j'=\frac{1}{2} \\ m_j'=-\frac{1}{2} \end{array} \begin{array}{c} \begin{array}{cc} m_j=\frac{1}{2} & m_j=-\frac{1}{2} \end{array} \\ \begin{pmatrix} i\beta E\sin\theta & -i\beta E\cos\theta \\ -i\beta E\cos\theta & -i\beta E\sin\theta \end{pmatrix} \end{array}. \tag{14}$$

Combining (12), (13), and (14) we obtain the total transition matrix in the F,m_F basis

$$= \begin{array}{c} \\ \langle 7^2P_{1/2},00| \\ \langle 11| \\ \langle 10| \\ \langle 1-1| \end{array} \begin{array}{c} \begin{array}{cccc} |6^2P_{1/2},00\rangle & |11\rangle & |10\rangle & |1-1\rangle \end{array} \\ \begin{pmatrix} 0 & iD-M_c & iH-M_s & -iD+M_c \\ iD-M_c & iH-M_s & -iD+M_c & 0 \\ iH-M_s & -iD+M_c & 0 & -iD+M_c \\ -iD+M_c & 0 & -iD+M_c & -iH+M_s \end{pmatrix} \end{array}, \tag{15}$$

where

$$H=\beta E\sin\theta-(\mathrm{Im}\mathscr{E}_P)\cos\theta\,,$$

$$D=\frac{1}{\sqrt{2}}[\beta E\cos\theta+(\mathrm{Im}\mathscr{E}_P)\sin\theta]\,,$$

$$M_s=M\sin\theta\,,$$

and

$$M_c=\frac{1}{\sqrt{2}}M\cos\theta\,.$$

Next we consider the effect of the external magnetic field B (See Fig. 3). It is chosen at 3.2 kG in order to resolve sufficiently the various Zeeman components of the 293-nm transition in spite of Doppler width [the full width at half maximum (FWHM) is $\Delta\nu_D\simeq 1.6$ GHz]. In particular, B is chosen to minimize the overlap of adjacent $\Delta m_F=0$ and $\Delta m_F=\pm 1$ components, which contain PNC terms of opposite sign, as we shall see momentarily. In finite B the eigenstates of Fig. 3 are expressed in terms of the F,m_F basis as follows:

State	Zeeman energy
$\|1,1\rangle$	$E_{11}=h\,\Delta\nu(1+\frac{1}{2}x)$
$\|+\rangle=\delta\,\|1,0\rangle+\gamma\,\|0,0\rangle$	$E_+=\frac{1}{2}h\,\Delta\nu[1+(1+x^2)^{1/2}]$
$\|1,-1\rangle$	$E_{1,-1}=h\,\Delta\nu(1-\frac{1}{2}x)$
$\|-\rangle=\delta\,\|0,0\rangle-\gamma\,\|1,0\rangle$	$E_-=\frac{1}{2}h\,\Delta\nu[1-(1+x^2)^{1/2}]$

(16)

where $h\Delta\nu_{6,7}$ is the hyperfine splitting between $F=1$ and $F=0$ for $n=6$ or 7, $x_{6,7}\cong\mu_0 g_J B/h\Delta\nu_{6,7}$, $g_J(^2P_{1/2})=\frac{2}{3}$, and

$$\delta=\frac{x}{\{x^2+[1-(1+x^2)^{1/2}]^2\}^{1/2}}\,, \tag{17}$$

$$\gamma=\frac{(1+x^2)^{1/2}-1}{\{x^2+[1-(1+x^2)^{1/2}]^2\}^{1/2}}\,. \tag{18}$$

From Eqs. (15)–(18), we compute the frequencies and transition probabilities for all possible pairs of levels between $6P_{1/2}$ and $7P_{1/2}$ in Fig. 3. Taking into account terms in β^2E^2 and $(\mathrm{Im}\mathscr{E}_P)\beta E$ (the latter is the PNC-Stark interference), but ignoring terms in M^2 and $(\mathrm{Im}\mathscr{E}_P)^2$, we obtain the results of Table I.

The Zeeman components selected for observation in

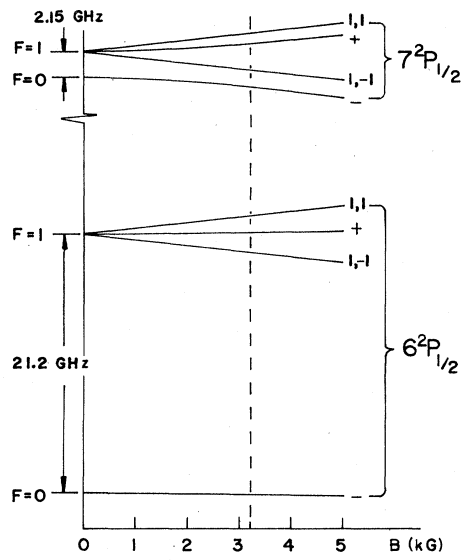

FIG. 3. Zeeman splittings of the $6P_{1/2}$ and $7P_{1/2}$ thallium states, to scale. States not mixed by the magnetic field are labeled F, m_F. States labeled $\pm$ are those for which $m_J=\pm\frac{1}{2}$, respectively, in the limit of large B.

this experiment are

$$\begin{aligned} &6^2P_{1/2}\rightarrow 7^2P_{1/2} \\ &|1,-1\rangle\rightarrow|1,-1\rangle\ ,\quad \Delta m_F=0\ ; \\ &|1,1\rangle\rightarrow|1,1\rangle\ ,\quad \Delta m_F=0\ ; \\ &|1,-1\rangle\rightarrow|+\rangle\ ,\quad \Delta m_F=1\ . \end{aligned} \tag{19}$$

At the peak of the resonance dominated by $|1,-1\rangle\rightarrow|1,-1\rangle$; $|1,1\rangle\rightarrow|1,1\rangle$ (which occur at the same frequency) there is some overlap of $|+\rangle\rightarrow|+\rangle$. Separated by 2.2 GHz is an adjacent peak containing mainly $|1,-1\rangle\rightarrow|+\rangle$ but with some overlap of $|+\rangle\rightarrow|1,1\rangle$. A scan of the line shape revealing all the nearby hyperfine transitions is shown in Fig. 4(a).

The transition probabilities for the two resonances indicated in (19) can be read directly from Table I. They are

$$\begin{aligned} T_{\Delta m_F=0} &\propto [\beta^2E^2\sin^2\theta-2(\mathrm{Im}\mathscr{E}_P)\beta E\sin\theta\cos\theta]\ , \\ T_{\Delta m_F=1} &\propto [\beta^2E^2\cos^2\theta+2(\mathrm{Im}\mathscr{E}_P)\beta E\sin\theta\cos\theta]\ . \end{aligned} \tag{20}$$

Equations (20) reveal explicitly the interference between the PNC and Stark amplitudes, and shows for these two particular components the general fact that $\Delta m_F=0$ and $\Delta m_F=\pm1$ transition probabilities contain Stark-PNC interference terms of opposite sign [See Fig. 4(b)]. Note also that for the geometry chosen here (see Fig. 2) there is no interference between M and $\mathscr{E}_P$ or between M and βE.

In the actual experiment, the $6^2P_{1/2}\rightarrow7^2P_{1/2}$ absorption is detected by observing the 535-nm fluorescence accompanying the decay $(7^2P_{1/2}\rightarrow)7^2S_{1/2}\rightarrow6^2P_{3/2}$ (see Fig. 1). The interference term, $2(\mathrm{Im}\mathscr{E}_P)\beta E\sin\theta\cos\theta$, is extracted by looking for an asymmetry

$$\Delta=\frac{T(+)-T(-)}{T(+)+T(-)}=\begin{cases} -\dfrac{2\,\mathrm{Im}\mathscr{E}_P}{\beta E}\cot\theta\ , & \Delta m_F=0 \\ +\dfrac{2\,\mathrm{Im}\mathscr{E}_P}{\beta E}\tan\theta\ , & \Delta m_F=\pm1\ , \end{cases} \tag{21}$$

TABLE I. Transition probabilities for $6^2P_{1/2}\rightarrow7^2P_{1/2}$ Zeeman components in external magnetic field B. The second column gives the transition strength, the third gives the sign and magnitude of the PNC-Stark interference term, and columns 4 and 5 give numerical values for frequencies splittings and relative line strengths for $B=3.2$ kG. The symbols used are defined as follows: [see Eqs. (16), (17), (18)]: $\omega=\delta_7\gamma_6+\delta_6\gamma_7$, $\omega'=\delta_7\delta_6-\gamma_7\gamma_6$, $\Lambda_{6\,(7)}=\delta_{6\,(7)}+\gamma_{6\,(7)}$, $\Gamma_{6\,(7)}=\delta_{6\,(7)}-\gamma_{6\,(7)}$. In this table we assume $\mathbf{E}=E\hat{\mathbf{y}}$, $\mathbf{B}=B\hat{\mathbf{z}}$, and perfect linear polarization. The complications arising from off-axis $\mathbf{E}$ and $\mathbf{B}$ components and imperfect linear polarization are discussed in Secs. II C and IV B.

$\Delta m_F=0$ transition	$E^2\beta^2\sin^2\theta$	$2(\mathrm{Im}\mathscr{E}_P)\beta E\sin\theta\cos\theta$	Relative frequency (GHz)	Relative intensity
$11\rightarrow11$	1	-1	0	1
$1-1\rightarrow1-1$	1	-1	0	1
$+\rightarrow+$	ω^2	$-\omega^2$	0.7	0.266
$-\rightarrow-$	ω^2	$-\omega^2$	18.5	0.266
$+\rightarrow-$	ω'^2	$-\omega'^2$	-3.0	0.735
$-\rightarrow+$	ω'^2	$-\omega'^2$	22.2	0.735
$\Delta m_F=\pm1$ transition	$E^2\beta^2\cos^2\theta$	$2(\mathrm{Im}\mathscr{E}_P)\beta E\sin\theta\cos\theta$	Relative frequency (GHz)	Relative intensity
$11\rightarrow-$	$\frac{1}{2}\Lambda_7^2$	$\frac{1}{2}\Lambda_7^2$	-4.4	0.905
$1-1\rightarrow+$	$\frac{1}{2}\Lambda_7^2$	$\frac{1}{2}\Lambda_7^2$	2.2	0.905
$+\rightarrow1-1$	$\frac{1}{2}\Lambda_6^2$	$\frac{1}{2}\Lambda_6^2$	-1.6	0.570
$-\rightarrow11$	$\frac{1}{2}\Lambda_6^2$	$\frac{1}{2}\Lambda_6^2$	22.9	0.570
$11\rightarrow+$	$\frac{1}{2}\Gamma_7^2$	$\frac{1}{2}\Gamma_7^2$	-0.7	0.095
$1-1\rightarrow-$	$\frac{1}{2}\Gamma_7^2$	$\frac{1}{2}\Gamma_7^2$	-1.4	0.095
$-\rightarrow1-1$	$\frac{1}{2}\Gamma_6^2$	$\frac{1}{2}\Gamma_6^2$	19.9	0.431
$+\rightarrow11$	$\frac{1}{2}\Gamma_6^2$	$\frac{1}{2}\Gamma_6^2$	1.4	0.431

where $T(\pm)$ refers to the transition probability (as measured by 535-nm intensity) for two coordinate systems of opposite handedness, defined by the relative orientations of $\hat{\boldsymbol{\varepsilon}}$, **E**, and **B**. In particular, the interference term reverses sign as θ or **E** is reversed, but remains unchanged under reversal of **B**. We choose $\theta=\pm 35°$ so that the signal sizes for the two transitions of (19) are approximately equal (see Fig. 4).

C. The effects of misalignment, imperfect linear polarization, line overlap, and imperfect field reversal

In the actual experimental apparatus **E** is not exactly parallel to $\hat{\mathbf{k}}$, nor is **B** exactly orthogonal to $\hat{\mathbf{k}}$ and **E**, nor are the photons in a state of perfect linear polarization. Moreover, the electric field does not reverse exactly. These imperfections result in interference terms in the transition probability that change sign with reversal of **E** or θ in the same way as PNC. The experimental methods we employ to isolate and eliminate such effects are discussed in Sec. IV B. (In fact the undesirable effects turn out to be very small.) Here we limit ourselves to a description of how the transition probabilities themselves must be modified.

First we must redefine the coordinate system. Let the photon wave vector **k** be parallel to $\hat{\mathbf{y}}$ and define the z axis as that which bisects the angle between "$+\theta$" and "$-\theta$" linear polarization. In this case **B** in general has off-axis components:

$$\mathbf{B}=B_x\hat{\mathbf{x}}+B_y\hat{\mathbf{y}}+B_z\hat{\mathbf{z}} \tag{22}$$

with $B_x,B_y \ll B_z$. The electric field is also misaligned in general:

$$\mathbf{E}=E_x\hat{\mathbf{x}}+E_y\hat{\mathbf{y}}+E_z\hat{\mathbf{z}}\ , \tag{23}$$

with

$$E_x,E_z \ll E_y\ .$$

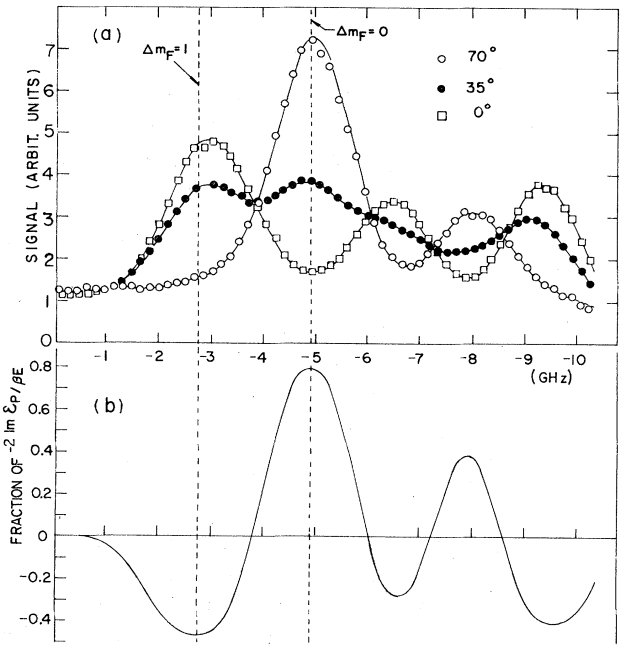

FIG. 4. (a) Laser scan of $6^2P_{1/2}$, $F=1\rightarrow 7^2P_{1/2}$, $F=1$ transition for $B=3.2$ kG, $\theta=0°$, 35°, 70°. The solid curves are theoretical. The dashed vertical lines indicate where parity data are taken (for $\Delta m_F=0$, -4.9 GHz; for $\Delta m_F=1$, -2.7 GHz). Data taken at $E=188$ V/cm. (b) Parity violating asymmetry vs frequency for $6^2P_{1/2}$, $F=1\rightarrow 7^2P_{1/2}$, $F=1$ transitions. The ordinate scale indicates the fraction of $-2\mathrm{Im}\mathscr{E}_P/\beta E$ expected.

We first modify (14) to include terms proportional to E_x and E_z. Using the following notation

$$\alpha_1=\alpha E_x\ ,\quad \alpha_2=\alpha E_y\ ,\quad \alpha_3=\alpha E_z\ ,$$
$$\beta_1=\beta E_x\ ,\quad \beta_2=\beta E_y\ ,\quad \beta_3=\beta E_z\ , \tag{24}$$

and also (8), we find that (14) becomes

$$\langle E1\rangle_{\text{Stark}}=\begin{array}{c} \\ m_j'=\frac{1}{2} \\ m_j'=-\frac{1}{2}\end{array}\begin{array}{c}\begin{array}{cc} m_j=\frac{1}{2} & m_j=-\frac{1}{2}\end{array}\\ \begin{pmatrix} i\beta_2\sin\theta+\alpha_1\sin\theta+\alpha_3\cos\theta & -i\beta_2\cos\theta+\beta_1\cos\theta-\beta_3\sin\theta \\ -i\beta_2\cos\theta-\beta_1\cos\theta+\beta_3\sin\theta & -i\beta_2\sin\theta+\alpha_1\sin\theta+\alpha_3\cos\theta\end{pmatrix}\end{array}\ . \tag{25}$$

To take into account the fact that the incoming photons (with nominal linear polarization) actually possess some degree of elliptical polarization, we write

$$\hat{\boldsymbol{\varepsilon}}=\hat{\mathbf{z}}\cos\theta+e^{i\eta}\hat{\mathbf{x}}\sin\theta\simeq\hat{\mathbf{z}}\cos\theta+(1+i\eta)\hat{\mathbf{x}}\sin\theta\ , \tag{26}$$

where η is a small real number. When expressions (25) and (26) are employed, the zero-magnetic-field transition amplitudes of (15) are modified as follows:

$$\langle 7^2P_{1/2},F',m_F'\,|\,(E1)_{\text{Stark}}+(E1)_{\text{PNC}}+(M1)\,|\,6^2P_{1/2},F,m_F\rangle$$

$$=\begin{array}{c}\\ \langle 7^2P_{1/2},00| \\ \langle 11| \\ \langle 10| \\ \langle 1-1|\end{array}\begin{array}{c}\begin{array}{cccc}|6^2P_{1/2},00\rangle & |11\rangle & |10\rangle & |1-1\rangle\end{array}\\ \begin{pmatrix} A' & C'+iD-M_c & iH'-M_s' & C'-iD+M_c \\ -C'+iD-M_c & A'+iH'-M_s' & C'-iD+M_c & 0 \\ iH'-M_s' & -C'-iD+M_c & A' & C'-iD+M_c \\ -C'-iD+M_c & 0 & -C'-iD+M_c & A'-iH'+M_s'\end{pmatrix}\end{array}\ , \tag{27}$$

where D and M_c are as previously defined [see Eq. (15)], and

$$A'=(1+i\eta)\alpha_1\sin\theta+\alpha_3\cos\theta\ ,$$

$$H=(1+i\eta)\beta_2\sin\theta-\mathrm{Im}\mathscr{E}_P\cos\theta\ ,\quad M_s'=(1+i\eta)M\sin\theta\ ,$$

and

$$C'=\frac{1}{\sqrt{2}}[\beta_1\cos\theta-(1+i\eta)\beta_3\sin\theta]\ .$$

Next we consider the effect of the misaligned **B** field. Starting with the states $|11\rangle$, $|+\rangle$, $|1-1\rangle$, $|-\rangle$ as defined in (16) we employ perturbation theory to calculate the changes in these states to first order in B_x, B_y. This yields the perturbed transition amplitude

$$\mathscr{A}'_{11\to11}=\mathscr{A}_{11\to11}+q_-\mathscr{A}_{11\to10}+q_+\mathscr{A}_{10\to11}\ , \tag{28}$$

and so on for the other $\Delta m_F=0$ and $\Delta m_F=\pm1$ transitions, where the $\mathscr{A}_{11\to11}$, $\mathscr{A}_{11\to10}$, etc., are given by Eq. (27) and $q_\pm=\frac{1}{2}(q_x\pm iq_y)$, with

$$q_x=B_x/B_z\ , \tag{29}$$

$$q_y=B_y/B_z\ . \tag{30}$$

From these results we construct the transition probabilities, including off-axis **E** and **B** components and imperfect linear polarization.

In addition to the terms already present in Table I, the transition probability for each component now contains additional terms in $\cos^2\theta$, $\sin^2\theta$, and in $\sin\theta\cos\theta$. The additional terms in $\cos^2\theta$ or $\sin^2\theta$ present no difficulty, however, because we require that the PNC asymmetry be odd under the reversal $\theta\to-\theta$, and our coordinate system is defined so that $\theta\to-\theta$, exactly. Table II displays the interference terms proportional to $\sin\theta\cos\theta$ for each Zeeman component, including all effects of second order or less in small quantities η, $q_x=B_x/B_z$, etc. With the exception of terms proportional to M, all undesirable interference terms are quadratic in E. Therefore, if the electric field were to reverse exactly, such terms would make no contribution to PNC. They are a source of difficulty only because in any real apparatus, the **E** reversal is imperfect. Let

$$\pm\mathbf{E}=(\pm E_{0x}+\Delta E_x)\hat{\mathbf{x}}+(\pm E_{0y}+\Delta E_y)\hat{\mathbf{y}}+(\pm E_{0z}+\Delta E_z)\hat{\mathbf{z}}\ , \tag{31}$$

where $E_{0x,0y,0z}$ are the reversing, and $\Delta E_{x,y,z}$ the nonreversing components of **E**. Any product of electric field components then contains two portions—one reversing and one nonreversing under reversal of the electric field. For example,

$$\alpha_1\alpha_3=\alpha^2(E_{0x}+\Delta E_x)(E_{0z}+\Delta E_z)=\alpha^2(E_{0x}E_{0z}+\Delta E_x\,\Delta E_z)+\alpha^2(E_{0x}\,\Delta E_z+E_{0z}\Delta E_x)\ . \tag{32}$$

The quantity $\alpha_1\alpha_3\sin\theta\cos\theta$ is odd under both reversal of θ and **E** and therefore has the same signature as PNC. In this fashion each of the interference terms listed in Table II can cause a false PNC asymmetry.

Since transitions $11\to11$ and $1-1\to1-1$ occur together at the same frequency, we simply add $T'(11\to11)$ and $T'(1-1\to1-1)$ to find the net transition rate for these two components. In this sum there is a cancellation of the terms in α_3M and $\eta B_2\alpha_3$. However, as already noted, in the actual experiment, each resonance-line component has finite Doppler width. Thus at $B=3.2$ kG there is some overlap of various Zeeman components (see Fig. 4), and in

TABLE II. Transition probabilities as in Table I, but with off-axis E and B field components and imperfect linear polarization taken into account. In addition to symbols already defined, the quantities $\rho=\delta_7\delta_6+\gamma_7\gamma_6$, $\rho'=\delta_7\gamma_6-\gamma_7\delta_6$ appear.

		(Interference terms)$\times(\sin\theta\cos\theta)$						
		$\beta_2^2\sin^2\theta$	$(2\beta_2\mathrm{Im}\mathscr{E}_P)$	$2\alpha_1\alpha_3$	$2\alpha_3M$	$2\beta_1\beta_2q_y$	$2\beta_2^2q_x$	$2\eta\beta_2\alpha_3$
$\Delta m_F=0$	$T'(11\to11)$	1	-1	$+1$	-1	$+1$	-1	-1
	$T'(1-1\to1-1)$	1	-1	$+1$	$+1$	$+1$	-1	$+1$
	$T'(+\to+)$	ω^2	$-\omega^2$	$+\rho^2$	$-\rho\omega$	$+\omega^2$	$-\omega^2$	$-\rho\omega$
	$T'(-\to-)$	ω^2	$-\omega^2$	$+\rho^2$	$+\rho\omega$	$+\omega^2$	$-\omega^2$	$+\rho\omega$
	$T'(+\to-)$	ω'^2	$-\omega'^2$	$+\rho'^2$	$-\rho'\omega'$	$+\omega'^2$	$-\omega'^2$	$-\rho'\omega'$
	$T'(-\to+)$	ω'^2	$-\omega'^2$	$+\rho'^2$	$+\rho'\omega'$	$+\omega'^2$	$-\omega'^2$	$+\rho'\omega'$
		(Interference terms)$\times(\sin\theta\cos\theta)$						
		$\beta_2^2\cos^2\theta$	$(2\beta_2\mathrm{Im}\mathscr{E}_P)$	$2\beta_1\beta_3$	$2\beta_3M$	$2\beta_1\beta_2q_y$	$2\beta_2^2q_x$	$2\eta(\beta_2\beta_3+q_y\beta_2^2)$
$\Delta m_F=\pm1$	$T'(11\to-)$	$\frac{1}{2}\Lambda_7^2$	$+\frac{1}{2}\Lambda_7^2$	$-\frac{1}{2}\Lambda_7^2$	$+\frac{1}{2}\Lambda_7^2$	$-\frac{1}{2}\Lambda_7^2$	$+\frac{1}{2}\Lambda_7^2$	$-\frac{1}{2}\Lambda_7^2$
	$T'(1-1\to+)$	$\frac{1}{2}\Lambda_7^2$	$+\frac{1}{2}\Lambda_7^2$	$-\frac{1}{2}\Lambda_7^2$	$-\frac{1}{2}\Lambda_7^2$	$-\frac{1}{2}\Lambda_7^2$	$+\frac{1}{2}\Lambda_7^2$	$+\frac{1}{2}\Lambda_7^2$
	$T'(+\to1-1)$	$\frac{1}{2}\Lambda_6^2$	$+\frac{1}{2}\Lambda_6^2$	$-\frac{1}{2}\Lambda_6^2$	$+\frac{1}{2}\Lambda_6^2$	$-\frac{1}{2}\Lambda_6^2$	$+\frac{1}{2}\Lambda_6^2$	$-\frac{1}{2}\Lambda_6^2$
	$T'(-\to11)$	$\frac{1}{2}\Lambda_6^2$	$+\frac{1}{2}\Lambda_6^2$	$-\frac{1}{2}\Lambda_6^2$	$-\frac{1}{2}\Lambda_6^2$	$-\frac{1}{2}\Lambda_6^2$	$+\frac{1}{2}\Lambda_6^2$	$+\frac{1}{2}\Lambda_6^2$
	$T'(11\to+)$	$\frac{1}{2}\Gamma_7^2$	$+\frac{1}{2}\Gamma_7^2$	$-\frac{1}{2}\Gamma_7^2$	$+\frac{1}{2}\Gamma_7^2$	$-\frac{1}{2}\Gamma_7^2$	$+\frac{1}{2}\Gamma_7^2$	$-\frac{1}{2}\Gamma_7^2$
	$T'(1-1\to-)$	$\frac{1}{2}\Gamma_7^2$	$+\frac{1}{2}\Gamma_7^2$	$-\frac{1}{2}\Gamma_7^2$	$-\frac{1}{2}\Gamma_7^2$	$-\frac{1}{2}\Gamma_7^2$	$+\frac{1}{2}\Gamma_7^2$	$+\frac{1}{2}\Gamma_7^2$
	$T'(-1\to1-1)$	$\frac{1}{2}\Gamma_6^2$	$+\frac{1}{2}\Gamma_6^2$	$-\frac{1}{2}\Gamma_6^2$	$+\frac{1}{2}\Gamma_6^2$	$-\frac{1}{2}\Gamma_6^2$	$+\frac{1}{2}\Gamma_6^2$	$-\frac{1}{2}\Gamma_6^2$
	$T'(+\to11)$	$\frac{1}{2}\Gamma_6^2$	$+\frac{1}{2}\Gamma_6^2$	$-\frac{1}{2}\Gamma_6^2$	$-\frac{1}{2}\Gamma_6^2$	$-\frac{1}{2}\Gamma_6^2$	$+\frac{1}{2}\Gamma_6^2$	$+\frac{1}{2}\Gamma_6^2$

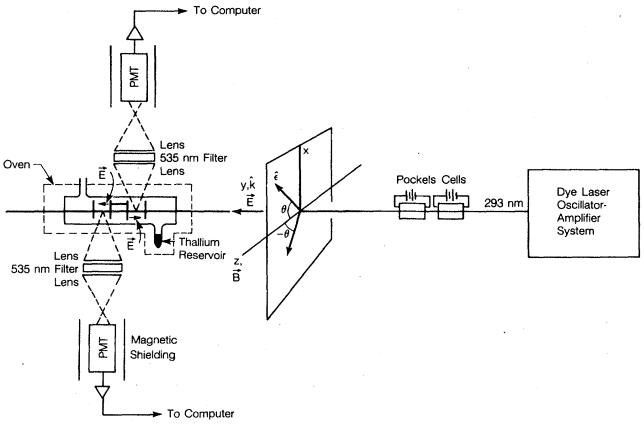

FIG. 5. Schematic diagram of the experiment.

particular at the center of the $11\rightarrow 11$ line there is about 10% overlap from the $+\rightarrow +$ line. Therefore, in the $11\rightarrow 11$, $1-1\rightarrow 1-1$ line as well as the $1-1\rightarrow +$ line, there is some contribution from each of the undesirable terms of Table II.

We note that by definition, $\hat{\mathbf{k}}$ is along $\hat{\mathbf{y}}$, and the principal component of $\mathbf{B}$ is along $\hat{\mathbf{z}}$. Thus, reversal of $\mathbf{B}$ is equivalent to change of sign of x as well as z. Consequently under $\mathbf{B}$ reversal, $E_{0x,z}$, $\Delta E_{x,z}$, and q_y change sign, while E_{0y}, ΔE_y in each region, and q_x remain unchanged. Thus the terms proportional to βM and ηB^2 or $\eta\alpha\beta$ in Table II change sign under $\mathbf{B}$ reversal while the remaining terms are unchanged. This, in addition to methods to be described in Sec. IV B, provides a means for isolating and eliminating the unwanted terms.

III. EXPERIMENTAL METHOD

Figure 5 is a schematic diagram of the experimental apparatus. The individual components will now be described in detail along with results from several experiments to calibrate the system.

A. Apparatus

The 293-nm light beam that stimulates the $6^2P_{1/2}\rightarrow 7^2P_{1/2}$ transition is generated by a dye-laser oscillator-amplifier system (Fig. 6). An actively stabilized cw dye laser (Coherent Inc. 599-21) pumped by an argon-ion laser (Coherent Inc. CR-6) is used as an oscillator at 585 nm, and the output ($\sim$40 mW) is amplified in three single-pass dye amplifiers pumped by the frequency-doubled output of a Q-switched Nd:YAG (neodymium: yttrium aluminum garnet) laser (Quanta Ray DCR-1 Oscillator).[12] The amplifier chain operates with Rhodamine 610 (Exiton) dissolved in methanol in concentrations of 145 mg/l in the first two transversely pumped amplifier cells and 25 mg/l in the final longitudinally pumped cell. The laser system produces 5 nsec, 2—3-MW pulses of 585-nm light in a bandwidth of $\sim$100 MHz with a repetition rate of 17 Hz. The beam spot is approximately 3 mm in diameter. This visible beam goes unfocused into an angle-tuned KD*P (deuterated potassium dihydrogen phosphate) crystal (Cleveland Crystals $12\times 12\times 30$ mm^3) and 293-nm uv light is generated with $\sim$30% efficiency. The visible and uv beams are separated by a fused-silica Brewster angle prism. Due to the phase-match condition of the doubling crystal the uv beam has horizontal polarization (along $\hat{\mathbf{z}}$) of high purity.

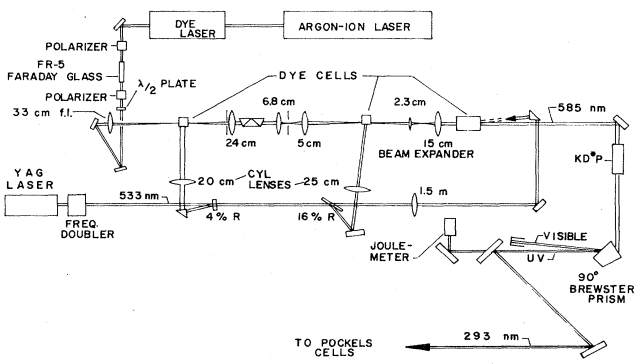

FIG. 6. Schematic diagram of the laser system used to generate 2927-Å light.

Two mirrors direct the uv beam through two Pockels cells and into the vacuum chamber containing the thallium-vapor cell. The alignment of the beam is monitored by an aperture at the entrance of the vacuum chamber and a grid on a wall 5 m away, and the beam can be aligned reproducibly within a fraction of a milliradian.

The two Pockels cells in series are each used as fixed half-wave plates to produce rotation of the plane of laser polarization $\hat{\boldsymbol{\epsilon}}$ when a voltage pulse (1.6 kV) is applied. The effective fast axis of the Pockels cells I and II (PCI and PCII) are set at angles θ and $\theta/2$ with the z axis, respectively, which gives four possible choices for the direction of linear polarization incident on the thallium cell:

PCI	PCII	Φ=angle between $\hat{\boldsymbol{\epsilon}}$, z axis
OFF	OFF	0
ON	OFF	2θ
OFF	ON	θ
ON	ON	$-\theta$

Data are taken at $\Phi=\pm\theta$ to observe PNC, where $\theta=35°$ is chosen to obtain approximate equality of the intensities of the $\Delta m_F=0$ and $\Delta m_F=1$ transitions of interest. Data at $\Phi=0°$, $\Phi=2\theta=70°$ are used to lock the cw laser (see Sec. III B 3) to the peak of the resonance in a computer-controlled feedback loop. For auxiliary experiments to measure systematic effects, PCII can be adjusted to give circular polarization of $+$ or $-$ helicity for $+$ or $-$ voltage applied to the PC electrodes. PCI is left unchanged for these measurements.

The Pockels cells are 10-mm-diam$\times$30-mm-long KD*P crystal (Cleveland Crystals QX 1020), specially selected for high-uv transmission. Both Pockels cells are supported on vertical and horizontal translation stages and a rotating mount for final alignment and small adjustments of the polarization. A reflection from the face

of PCI is directed with a mirror into a pyroelectric joulemeter (Molectron J-3) so that the uv beam energy can be monitored. The quality and orientation of $\hat{\varepsilon}$ are checked by passing the beam through a (Glan-air) prism on a rotating mount and into a photodiode. The ratio of transmission when the polarizer is parallel to $\hat{\varepsilon}$ to extinction when it is perpendicular is always better than 10^3 for all choices of linear polarization both before and after the beam has passed through all the optical elements in the system, including the thallium cell and vacuum-can windows. The angle Φ can be determined by the angle marks on the polarizer mount to $\pm 1°$. Finer adjustments of Φ are made later, by means of the thallium atoms themselves.

The final optical element through which the beam passes before entering the vacuum can and thallium cell is a thin quartz plate which can be tilted and rotated independently. Without this plate, the intensity of light in the thallium cell with $\Phi = +\theta$ is 0.5% greater than the intensity of light with $\Phi = -\theta$. By adjusting the angle of the plate we equalize the intensities of the light for $\Phi = \pm\theta$ to better than 0.03%. Due to the scattering and reflection losses in the Pockels cells, we typically operate with 1.5—2.0 mJ per laser pulse of beam energy at the entrance to the vacuum system.

The magnetic field is provided by an electromagnet (originally used for NMR) with 30-cm-diam pole tips and a 15.9-cm gap. The magnet provides a homogeneous field of up to 5 kG that varies in magnitude by less than 0.3% over the central region (12-cm-diam) where the experiment takes place. The field is measured by a Hall probe and monitored continuously while the experiment is in progress. Mounted within the magnet gap is an aluminum vacuum chamber containing the thallium-vapor cell and its surrounding electrically heated oven, normally operated at about 950 K, at which the vapor density is $\sim 5\times 10^{14}$ cm^{-3} and the Doppler width of the $6^2P_{1/2}$-$7^2P_{1/2}$ transition is 1.6 GHz. The entire vacuum chamber can be rotated in the magnet gap about the x axis (see Fig. 2) by up to 0.010 radians for alignment and measurement of systematic effects.

The thallium-vapor cell is shown in Fig. 7. The body of the cell is a fused-silica cylinder, 48-mm o.d. with 2.5-mm wall thickness. A 7-cm-long stem of 1.0-cm-o.d.

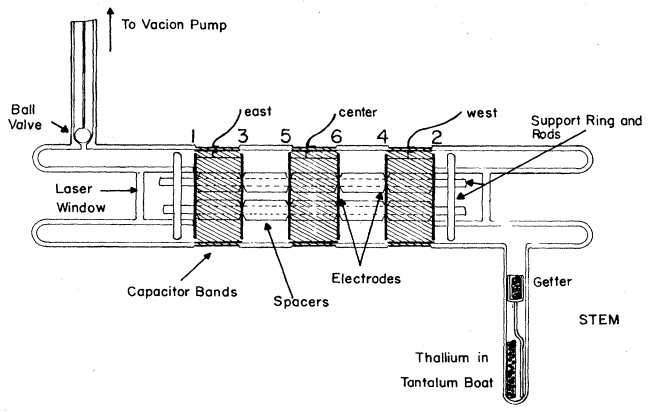

FIG. 7. Diagram of the thallium-vapor cell.

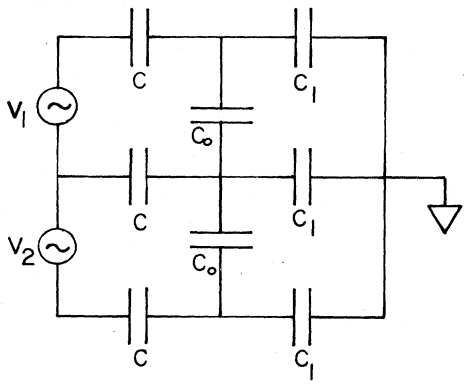

FIG. 8. Equivalent circuit for electric field pulser and interaction regions. C: band capacitances (33 pf); C_0: interaction region electrode capacitances; C_1: stray capacitances to ground. The latter are not all equal *a priori*, but in fact turn out to be within the uncertainty stated in the text.

fused-silica tubing contains the metallic ^{205}Tl (99.44% ^{205}Tl, 0.56% ^{203}Tl) in a reservoir. This stem is heated separately from the main body of the cell and is typically kept at ~875 K. The cell is evacuated by a Vacion pump (Varian) through a remotely activated quartz ball valve. The cell and windows through which the laser beam passes are Suprasil quartz desks (Amersil), 3-mm thick, in reentrant holders. The windows are annealed after they are sealed to the window holders to reduce birefringence, and the final cell seal attaching the window holder to the cell body is made far enough from the window not to introduce any additional stress. The end of each window holder is ground parallel to the window it contains. Care is taken to keep the cell windows parallel to each other and after assembly the relative tilt between the windows is approximately 3 mrad.

The cell contains six coaxial nickel-disk electrodes, 4 cm in diameter and 1-mm thick. Each disk has a 12-mm-diam center hole for the laser beam to pass through. The electrodes are supported on four quartz rods and separated by quartz spacers ground to a precision of 0.0025 cm. The ends of the window holders support the electrode assembly and provide a flat reference surface parallel to the windows for alignment of the electrodes within the cell. The six electrodes are electrically connnected in pairs (1 and 3, 5 and 6, and 4 and 2 are connected) and each of the three pairs has an independent potential applied to it. Electrodes 1 and 2 serve to smooth the electric field and baffle scattered laser light from the two interaction regions defined by electrodes 3,5 and 4,6. During data acquisition, the outer pairs of electrodes are kept at approximately equal potentials and the center pair is at the opposite potential, so that the electric fields in the two interaction regions are equal and opposite. The interaction regions defined by the electrodes are each 22-mm long and their centers are separated by 4.0 cm. The entire electrode assembly is 10-cm long.

The electrodes are coupled capacitively to an external pulser with 80-nsec pulses by three pairs of 2-cm-wide bands of tantalum foil, one inside and one outside the cell. Each inner band is 0.025-cm thick and stiff enough to

spring out against the inner cell wall. Each outer band is 0.010-cm thick and is held in place with a spring. The quartz cell wall between the bands is ground to 0.15-cm thickness to form a seat for the bands and to increase the capacitance. The location of the bands is shown in Fig. 7 and the capacitance of each band is measured to be 33 pF. A schematic diagram of the equivalent circuit is shown in Fig. 8.

Although each interaction region is defined by electrodes separated by 22 mm, only the center 10 mm of each interaction region is viewed by each detector. In order to determine the average electric field over this effective length, two factors must be taken into account. First, the center hole and finite electrode diameters diminish the value of the field from the value one would expect with two infinite parallel plates with potentials $\pm V/2$ applied to them. These geometric effects are taken into account by solving Laplace's equation numerically by computer, subject to the actual electrode, cell, and oven boundary conditions. The fractional precision of the solution is about 3 parts in 10^3. It reveals that the average value of E_{0y} over the effective interaction length in each region is smaller by 8% than that which would be obtained with infinite parallel plates at the same voltage. A second correction must be applied to account for capacitive coupling (see Fig. 8). The capacitance of the interaction regions C_0 as well as the stray capacitance to ground C_1 shunt the band capacitance $C=33$ pF. The ratio of the voltage V_{10}, appearing across the electrodes in a given interaction region, to the voltage $V=V_1=V_2$ applied between the external capacitor bands may be shown from analysis of the circuit of Fig. 8 to be

$$\left.\frac{V_{10}}{V}\right|_a \cong 1-\frac{C_1}{C}-\frac{3C_0}{C}\ , \quad V=V_1=V_2\ . \tag{33}$$

If the voltages in the two regions are made unequal by grounding one of the outer capacitor bands, so that $V_1=V$, and $V_2=V/2$, then Eq. (33) is modified:

$$\left.\frac{V_{10}}{V}\right|_b \cong 1-\frac{C_1}{C}-\frac{5C_0}{2C}\ , \quad V_1=V\ , \quad V_2=V/2\ . \tag{34}$$

Experimentally, the quantity

$$\frac{V_{10}/V\,|_a}{V_{10}/V\,|_b}=\frac{V_{10,a}}{V_{10,b}}\cong 1-\frac{1}{2}\frac{C_0}{C}\ , \tag{35}$$

is measured by observing the signal size in one region (proportional to E^2) as the outer electrode in the other region is switched from potential $V/2$ to ground. Using this method we find $C_0/C=-0.019$. C_1, the stray capacitance to ground, cannot be measured very precisely and must be calculated from the known geometry and standard electrostatics. We find $C_1=3.2\pm1.0$ pF, where the uncertainty here is very conservative. We conclude that the electric field in the interaction region is diminished by a factor 0.845 because of capacitive coupling. The uncertainty in the effective electric field, $\pm3\%$, is dominated by the uncertainty in C_1. Parity-nonconservation data were taken with $E=351$, 188, 109, and 67 V/cm.

The 535-nm fluorescence in each region from the decay $7^2S_{1/2}\rightarrow 6^2P_{3/2}$ passes through the cell wall, holes in the oven and heat shields, and water-cooled vacuum windows. A liquid filter of potassium acid phthalate dissolved in distilled H_2O (12 g/l) effectively blocks scattered 293-nm laser light.[13] The transmitted light is then collimated by a 10.2-cm f-1 Fresnel lens, passes through a 10.2-cm-diam, 535-nm interference filter (10-nm bandwidth, 60% peak transmission) and is refocussed by a second 10.2-cm Fresnel lens. An EMI 9658 photomultiplier tube, 3.8 cm behind the final lens focus, detects the 535-nm photons. Typically we collect about 10^5 photoelectrons per laser pulse in each tube. The tube outputs are integrated, amplified, digitized and stored in a Digital Equipment Corporation LSI-11/2 computer which controls the experiment in addition to recording and analyzing the data.

1. Backgrounds

Various sources contribute a background to the 535-nm-photon counting rate. These are as follows.

(a) Scattered laser light contributes about 2% of the signal at the peak of the $\Delta m_F=0$ resonance at 188 V/cm. It arises from 293-nm photons that generate fluorescence at 535 nm in cell walls and/or oven and vacuum windows. The direct transmission of 293-nm light through the phthalic acid filter is negligible.

(b) A broad nonresonant background that probably arises from Tl atom-atom collisions yields about 10% of the signal at the peak of the $\Delta m_F=0$ resonance at 188 V/cm. It increases with temperature more rapidly than the signal.

(c) An electric field-dependent background (roughly proportional to E^2) contributes about 10% of the $\Delta m_F=0$ resonance signal 188 V/cm. It has a number of possible causes, one being the ejection of electrons from cell surfaces by 293 nm photons. The electrons are accelerated in the E field and collide with Tl atoms, thus generating 535-nm fluorescence. A preliminary version of the cell was constructed with tantalum electrodes. Photoejection of electrons from the tantalum surfaces caused unacceptable background problems, because tantalum has a photoelectric threshold at about 300 nm. The new cell, with which all PNC data were obtained, contains nickel electrodes (photoelectric threshold $\sim$250 nm) and difficulties with background were reduced.

B. Data acquisition and processing

Three signals are sent to the computer with each laser pulse: N_1 and N_2 from the detectors viewing each region, and a third pulse from the laser beam power monitor. These are all binned according to sign (E), and sign (θ) which change from pulse to pulse. For each group of 16 pulses, four are taken in each of the configurations E, $\theta=++,+-,-+,--$, in an order assigned by the computer random-number generator. Once every 16 pulses, the polarization is switched to take two pulses of tuning data with $\theta=70°$ and 0° (see Sec. III B 3). This sequence is repeated 64 times to make a data point which is stored on disc and displayed. The laser is then automatically tuned from $\Delta m_F=0$ to $\Delta m_F=1$, or vice versa, and the sequence is repeated. The magnetic field is reversed

once every 16 groups of 1024 pulses. The data are combined as described in the following sections to measure PNC and systematic effects.

1. PNC channel data

The magnetic field **B** is nominally the same for both regions, as is the linear polarization $\hat{\epsilon}$, but the electric fields in the two regions are opposite; thus we nominally have $\mathbf{E}^{(1)}=-\mathbf{E}^{(2)}$. To collect PNC data we form a "region asymmetry"

$$\Delta_R=(N_1-N_2)/(N_1+N_2) \tag{36}$$

where N_1 and N_2 are the counts in detectors 1 and 2, respectively, and then we form, on-line,

$$\Delta_{\mathrm{PNC}}=\tfrac{1}{4}(\Delta^{++}-\Delta^{+-}-\Delta^{-+}+\Delta^{--}) \tag{37}$$

where Δ^{++}, etc. refer to Δ_R for the configurations E, $\theta=++,+-$, etc. The reason for using two independent regions and working with "region asymmetries" is to normalize out pulse-to-pulse laser intensity fluctuations, that would otherwise overwhelm the experiment.

Equal quantities of data are taken for each sign of **B**, and Δ_{PNC} is averaged over sign (B). Equal amounts of data are also taken on the two resonances $\Delta m_F=0$, and $\Delta m_F=1$. Since θ and B are such that the signals (and signal-to-background ratios) are the same for both resonances, these data can be combined to yield

$$\bar{\Delta}=\tfrac{1}{2}[\Delta(\Delta m_F=0)-\Delta(\Delta m_F=1)]\ . \tag{38}$$

Each time a data point is stored, a number of quantities averaged over 1024 pulses are recorded in addition to Δ_{PNC}: $N_1{}^{++}$, $N_2{}^{++}$, Δ^{++}, etc., along with their standard deviations. [Here $N_1{}^{++}$ refers to the counts in channel 1 with sign $(E)>0$, sign $(\theta)>0$, etc.] In an off-line program, the PNC data can then be analyzed independently for each region, for each sign (E) and for each sign (θ). In particular the PNC information from each individual region imposes important constraints on systematic corrections (see Sec. IV B).

2. Laser tuning

As is evident from Fig. 4, at $\theta=0°$, only $\Delta m_F=\pm1$ transitions are excited, while at 70°, the $\Delta m_F=0$ transitions dominate. The maximum PNC asymmetry occurs on the $\Delta m_F=0$ line when the ratio R of the intensity at 70° to that at 0° is a maximum. As noted, tuning data with $\theta=70°$ and 0° are taken about once per second. R is calculated, averaged over 16 measurements, and then compared with its previous value. An automatic feedback loop adjusts the laser frequency to maximize R for $\Delta m_F=0$ data. The frequency is then shifted by 2.2 GHz to where R is a maximum for $\Delta m_F=1$ data. The value of R on each resonance also yields an accurate and continuous measurement of the signal-to-background ratio (see Sec. IV A).

3. Resonance line profiles

We use the computer-controlled laser system to scan the resonance line in order to verify our understanding of the line shape. At a given frequency normalized signals for 64 pulses are averaged and the frequency is then shifted by 100 MHz. The resulting resonance curves are fitted by a sum of Gaussians. Data are taken with $B=0$ to measure the Doppler width and $7^2P_{1/2}$ hyperfine-structure (hfs) splitting, and to calibrate the scan rate. Data at $B=3.2$ kG are taken with $\theta=0°$ and 70°, as well as $\theta=35°$ (see Fig. 4). The resulting fitted values of B, θ, and the scan rate are in excellent agreement with independent measurements of these quantities and the fitted values of the Doppler width agrees well with that calculated from the cell temperature. Our determination of the $7^2P_{1/2}$ hfs splitting from the $B=0$ line profile:

$$\Delta\nu(7^2P_{1/2})=2.15\pm0.02\ \mathrm{GHz} \tag{39}$$

is more precise than the previous published measurement.[14]

IV. OBSERVATIONS

A total of 1.2×10^7 pulses of PNC data were accumulated. Four values of electric field were employed: $E=67$, 109, 188, and 351 V/cm. An overall data summary is given in Table III, which lists $\bar{\Delta}$ [see Eq. (38)], for each run, together with a statistical uncertainty, the value of E and the number of pulses in that run. We now consider two types of corrections to the data: first, those due to finite signal-to-background ratio; and second, those due to systematic false PNC terms (see Sec. II C).

TABLE III. Summary of data for parity runs at four different electric fields. The total number of laser pulses is given along with the average signal-to-background ratio and the fraction of $2\mathrm{Im}\mathscr{E}_P/\beta E$ expected from signal-to=background and line overlap dilution. The values of $\bar{\Delta}$ appearing in the table have been obtained by dividing the raw values by the corresponding factors appearing in the column "% of asymmetry expected."

Electric field (V/cm)	Number of pulses	$S(70°)/b$	% of asymmetry expected	$\bar{\Delta}$ ($\times10^{-7}$)
351	1 958 912	4.6	59	-104 ± 36
188	4 669 440	3.7	55	-156 ± 41
109	2 627 584	3.0	48	-328 ± 89
67	2 748 416	1.3	32	-504 ± 188

A. Background corrections

The sources of background were described in Sec. III A 2. The background presents two problems: first, it dilutes the asymmetry by a factor (signal)/(signal + background); and second, if the background itself depends on sign (E) and sign (θ) it can contribute a false PNC asymmetry. Two methods are used to determine the signal-to-background ratio. During PNC data acquisition, R (see Sec. III B 3) is monitored and recorded. Defining b as background, we have

$$R=\frac{S(70°)+b}{S(0°)+b} . \tag{40}$$

However, $S(70°)/S(0°)$ depends only on B and the Doppler width, and may be calculated. Thus (40) may be used to find $S(70°)/b$. This is checked by determining $S(70°)/b$ directly from the line profiles, which are fit to a signal plus background [see Fig. 4(a)]. It is then straightforward to calculate that fraction of $2\mathrm{Im}\mathscr{E}_P/\beta E$ one expects to observe for each transition, where the dilution arises from background as well as from neighboring Doppler-broadened lines. The same remarks apply for dilutions of false PNC asymmetries. The fraction of $2\,\mathrm{Im}\mathscr{E}_P/\beta E$ expected and $S(70°)/b$ are given in Table III. By taking equal amounts of data on the $\Delta m_F=0$ and $\Delta m_F=1$ transitions at angle $\theta=35°$, where

$$S/b \mid_{\Delta m_F=0} \cong S/b \mid_{\Delta m_F=1}$$

we effectively guard against possible systematic shifts due to a small dependence of background on sign (θ), sign (E).

B. Measurement of systematic effects

Table II summarizes all the interference terms which can masquerade as false PNC. It is useful to write down the total transition probability for a particular hyperfine component and explicitly include the systematic terms after the region and θ and E subtractions have been done. Recall that in the electric fields in the two interaction regions are equal and opposite: $\mathbf{E}^{(1)}=-\mathbf{E}^{(2)}$. We have (not including line overlap)

$$\begin{aligned}\Delta_{\mathrm{PNC}}(1-1\to+)=2\frac{\tan\theta}{\beta^2}&\frac{1}{(E_{0y}^{(1)2}+E_{0y}^{(2)2})}\\ &\times\{\beta(\mathrm{Im}\mathscr{E}_P)(E_{0y}^{(1)}+E_{0y}^{(2)})+\beta^2(E_{0z}^{(1)}\Delta E_x^{(1)}+E_{0x}^{(1)}\Delta E_z^{(1)}+E_{0x}^{(2)}\Delta E_z^{(2)}+E_{0z}^{(2)}\Delta E_x^{(2)})\\ &-\beta M(E_{0z}^{(1)}+E_{0Z}^{(2)})-\beta^2[(E_{0x}^{(1)}\Delta E_y^{(1)}+E_{0y}^{(1)}\Delta E_x^{(1)})q_y^{(1)}+(E_{0x}^{(2)}\Delta E_y^{(2)}+E_{0y}^{(2)}\Delta E_x^{(2)})q_y^{(2)}]\\ &+\beta^2(2E_{0y}^{(1)}\Delta E_y^{(1)}q_x^{(1)}+2E_{0y}^{(2)}\Delta E_y^{(2)}q_x^{(2)})+\eta\beta^2(E_{0y}^{(1)}\Delta E_z^{(1)}+E_{0z}^{(1)}\Delta E_y^{(1)}+E_{0y}^{(2)}\Delta E_z^{(2)}+E_{0z}^{(2)}\Delta E_y^{(2)})\} .\end{aligned} \tag{41}$$

The first term in parentheses is the true PNC contribution. To separate it from the other terms in (41) we independently determine or put limits on the quantities: E_{0z}, ΔE_z, E_{0x}, ΔE_x, and ΔE_y for each region separately and q_y, q_x, and η.

1. On-line limits

(a) *Linear polarization imperfections.* As noted in Sec. III A 1 the 293-nm linear polarization is checked periodically by extinction measurements with a high quality glan-air prism. We find

$$\eta\leq 0.03 , \tag{42}$$

where η is defined in (26).

(b) $q_x^{(1,2)}$ *and* $\Delta E_y^{(1,2)}/E_y$. During PNC data acquisition we monitor $q_x^{(1,2)}$ and $\Delta E_y^{(1,2)}/E_y$, continuously. Each time a data point is stored, four diagnostic quantities are calculated, stored, and displayed. They are

$$\gamma_E^{(1,2)}=\frac{N_{1,2}(+E)-N_{1,2}(-E)}{N_{1,2}(+E)+N_{1,2}(-E)} \tag{43}$$

and

$$\gamma_{\mathrm{uv}}^{(1,2)}=\frac{N_{1,2}(+\theta)-N_{1,2}(-\theta)}{N_{1,2}(+\theta)+N_{1,2}(-\theta)} . \tag{44}$$

Here 1,2 refer to the regions and $N_{1,2}(\pm E)$ refer to counts in channel 1 or 2 with $\pm E$ (averaged over $\pm\theta$), with a complementary definition for $N_{1,2}(\pm\theta)$. The quantity $\gamma_E^{1,2}$ is used to balance the E field in each region so that $|+E|=|-E|$. We recall that the leading term in the transition rate is proportional to

$$\beta_2^2\sin^2\theta \quad (\Delta m_F=0) ,$$

$$\beta_2^2\cos^2\theta \quad (\Delta m_F=1) ,$$

where $\beta_2=\beta(\pm E_{0y}+\Delta E_y)$. Thus from (43) we obtain

$$\gamma_E^{1,2}=\frac{2\Delta E_y^{(1,2)}}{E_{0y}^{(1,2)}} . \tag{45}$$

Online adjustments of the electric field pulser permit us to keep γ_E very small in both regions.

Similarly, it is easy to show from Table II that to leading order

$$\gamma_{\mathrm{uv}}^{(1,2)}=\begin{cases}-2q_x^{(1,2)}\cot\theta , & \Delta m_F=0 ,\\ +2q_x^{(1,2)}\tan\theta , & \Delta m_F=1 .\end{cases} \tag{46}$$

This quantity is proportional to B_x; thus by rotating Pockels cell II to minimize γ_{uv} we choose the laser polarization so as to minimize q_x. After correction for finite signal-to-background, we obtain

$$\left.\begin{aligned}\Delta E_y^{(1)}/E_{0y}^{(1)}\\ \Delta E_y^{(2)}/E_{0y}^{(2)}\end{aligned}\right\} < 10^{-4}\,, \tag{47,48}$$

$$\left.\begin{aligned}q_x^{(1)}\\ q_x^{(2)}\end{aligned}\right\} < 5\times 10^{-4}\,. \tag{49,50}$$

These limits ensure that contributions from terms of the form $\beta_2^2 q_x$ are negligible.

2. Circular polarization measurements

Interspersed among the PNC runs were three runs where the 293-nm beam was circularly polarized. This was done to magnify artificially and by about a factor of 30 the contribution of terms proportional to η in Table II [for example, see the last term in Eq. (41)]. When circularly polarized light is employed, the transition probability becomes, to leading order in terms odd under helicity reversal

$$T \propto \beta_2^2 \pm 2a\beta_2\alpha_3$$

or

$$T \propto \beta_2^2 \mp 2a\beta_2\beta_3\,, \tag{51}$$

where a is the appropriate coefficient from column 8 of Table II, and $\pm$ refers to helicity. In each case, the interference term is odd under b reversal. Using the definitions of $\Delta_{\rm PNC}$ and $\gamma^{\rm uv}$ [Eqs. (37) and (44), respectively] and adapting them in an obvious way for circular polarization, we find

$$\Delta_{\rm CP}^{(1,2)} \propto \frac{2\Delta E_z^{(1,2)}}{E_{0y}^{(1,2)}}\,, \tag{52}$$

$$\gamma_{\rm CP,uv}^{(1,2)} \propto \frac{2E_{0z}^{(1,2)}}{E_{0y}^{(1,2)}}\,, \tag{53}$$

where the constants of proportionality, dependent on line overlap, hfs mixing, and signal-to-background, are determined precisely from line-shape scans and routine calculation. In actuality, since $\Delta_{\rm CP}$ and $\gamma_{\rm CP,uv}$ are odd under B reversal we employ

$$\bar{\Delta}_{\rm CP} = \tfrac{1}{2}[\Delta_{\rm CP}(+B) - \Delta_{\rm CP}(-B)] \tag{54}$$

and similarly for $\bar{\gamma}_{\rm CP,uv}$.

Circular polarization data were obtained for $E = 67$ and 188 V/cm. Neither E_{0z}/E_{oy} nor $\Delta E_z/E_{0y}$ were found to vary with E. The results from the two values of E are thus combined and listed in Table IV. The uncertainties in the sums of off-axis E-field components are an order-of-magnitude smaller than for the differences, because in the former case we can take advantage of region subtraction [see Eq. (41)], while in the latter case laser intensity fluctuations are not canceled. The values of E_{0z} and ΔE_z in Table IV yield limits on the $\alpha_3 M$ and $\eta\beta_2\alpha_3$ (or $\beta_3 M$, $\eta\beta_2\beta_3$) contributions to false PNC asymmetry [see Table II or Eq. (41)]. Since both types of terms are odd under B reversal, each is suppressed by an additional factor of 20 (the accuracy to which we determine the B reversal).

3. Measurements with the vacuum chamber rotated

The vacuum chamber and cell can be rotated in the magnet gap by ± 0.010 rad. When this is done the laser beam is realigned to pass along the cell center axis, as always. The net effect of rotation is thus to introduce an artificially large $q_y = B_y/B_z$, and therefore to make false terms of the form $\beta_1\beta_2 q_y$ [see Eq. (41)] an order of magnitude larger than they would normally be for PNC data (where the tilt angle is less than 0.001 rad). The data obtained for large rotations is also used to determine $E_{0x}^{(1,2)}$ and $E_x^{(1,2)}$, directly. Combining such results with circular polarization data (Sec. IV B 2) we measure the contribution of false terms of the form $\alpha_1\alpha_3$ (or $\beta_1\beta_3$).

When q_y is large, the leading term in Δ is

$$\Delta(q_y) \propto \frac{2q_y}{E_{0y}}\left[\frac{E_{0x}^{(1)}+E_{0x}^{(2)}}{2}\frac{\Delta E_y}{E_{0y}} + \frac{\Delta E_x^{(1)}+\Delta E_x^{(2)}}{2}\right]. \tag{55}$$

By employing

$$\bar{\Delta}(q_y) = \tfrac{1}{2}[\Delta(q_y^+) - \Delta(q_y^-)]\,, \tag{56}$$

we retain that contribution which is odd under reversal of **B**, and discard that portion which contains a true PNC asymmetry. In order to extract information on both E_{0x} and ΔE_x, data with large q_y are taken with $\Delta E_y/E_{0y}$ set artificially large in both regions. (This is done by unbalancing the electric field pulser to give

TABLE IV. Measured values for off-axis and nonreversing components of the electric field.

$\frac{E_{0z}^{(1)}+E_{0z}^{(2)}}{2E_{0y}} = (5.9\pm 0.15)\times 10^{-4}$	$\frac{E_{0x}^{(1)}+E_{0x}^{(2)}}{2E_{0y}} = (2.6\pm 1.2)\times 10^{-3}$
$\frac{E_{0z}^{(1)}-E_{0z}^{(2)}}{2E_{0y}} = -(2.0\pm 1.4)\times 10^{-4}$	$\frac{E_{0x}^{(1)}-E_{0x}^{(2)}}{2E_{0y}} = -(2.6\pm 1.7)\times 10^{-3}$
$\frac{\Delta E_z^{(1)}+\Delta E_z^{(2)}}{2E_{0y}} = -(3.5\pm 0.16)\times 10^{-4}$	$\frac{\Delta E_x^{(1)}+\Delta E_x^{(2)}}{2E_{0y}} = (3.15\pm 2.1)\times 10^{-4}$
$\frac{\Delta E_z^{(1)}-\Delta E_z^{(2)}}{2E_{0y}} = -(0.6\pm 1.4)\times 10^{-4}$	$\frac{\Delta E_x^{(1)}-\Delta E_x^{(2)}}{2E_{0y}} \le 10^{-3}$
$\frac{\Delta E_y^{(1,2)}}{E_{0y}^{(1,2)}} \le 10^{-4}$	
$q_x^{(1,2)} \le 5\times 10^{-4}$	

$\Delta E_y/E_{0y}=\pm 0.12$.) By averaging $\bar{\Delta}(q_y)$ over $\Delta E_y/E_{0y}$ we measure $(\Delta E_x^{(1)}+\Delta E_x^{(2)})/E_{0y}$, while by taking the difference

$$\frac{1}{2}\left[\bar{\Delta}\left[q_y,\frac{\Delta E_y}{E_y}>0\right]-\bar{\Delta}\left[q_y,\frac{\Delta E_y}{E_y}<0\right]\right],$$

we extract $(E_{0x}^{(1)}+E_{0x}^{(2)})/E_{0y}$.

We obtained 3.6×10^6 pulses of data at $E=109$, 188, and 351 V/cm with the chamber rotated by ± 0.010 rad. Since the effects being measured were of the same order-of-magnitude as PNC, the results were limited by statistical uncertainty. We accumulated sufficient data to determine $(\Delta E_x^{(1)}+\Delta E_x^{(2)})/E_{0y}$ and $(E_{0x}^{(1)}+E_{0x}^{(2)})/E_{0y}$, and demonstrate that they do not vary with $|E|$. As in the case of the circular polarization measurements {Sec. IV B 2) the uncertainties in these sums of off-axis components are relatively small because of region subtraction [see (41)]. However, we cannot take advantage of region subtraction to determine $(\Delta E_x^{(1)}-\Delta E_x^{(2)})/E_{oy}$ and $(E_{ox}^{(1)}-E_{0x}^{(2)})/E_{0y}$. Instead, asymmetry data from the regions separately, which have large uncertainties due to laser intensity fluctuations, are used to place an upper limit on $(\Delta E_x^{(1)}-\Delta E_x^{(2)})/E_{0y}$. This number then becomes part of our systematic uncertainty. The quantity $(E_{ox}^{(1)}-E_{0x}^{(2)})/E_{0y}$ is determined by measuring the small deviation (~ 0.003 rad) of cell electrode planes from parallelism, with optical methods. This also yields a measurement of $(E_{0z}^{(1)}-E_{0z}^{(2)})/E_{0y}$ in excellent agreement with that obtained from circular polarization data (see Sec. IV B 2).

Table IV summarizes the measured values of electric field components. These are combined to yield values of the false PNC terms according to the entries of Table II and formulas analogous to Eq. (41) but also including the effects of line overlap dilution. The principal contributions to Δ^{false} arise from terms of the form $\alpha_1\alpha_3$ or $\beta_1\beta_3$. In fact, all other contributions are quite negligible. In particular, the only contribution to Δ^{false} with the same E dependence as the true PNC effect is that part proportional to M. Because of B cancellation, this portion of Δ^{false} is only about 1×10^{-7}. There remains the question of a possible false PNC contribution from dependence of the background on sign (E), sign (θ). To investigate this we took a considerable amount of data off resonance. When cancellation from switching between the two resonance lines, and other factors, are taken into account, this effect contributes at about the same level as the M portion of Δ^{false}.

Finally, then, the total measured contribution of all false PNC terms is

$$\begin{aligned}\Delta^{\text{false}}(\Delta m_F=0)&=(-15\pm 14)\times 10^{-7},\\ \Delta^{\text{false}}(\Delta m_F=1)&=(+5\pm 14)\times 10^{-7}.\end{aligned}\tag{57}$$

4. PNC results

The systematic corrections of Eq. (57) are applied separately to the observed asymmetries $\Delta(\Delta m_F=0)$ and $\Delta(\Delta m_F=1)$ after the latter have been corrected for finite signal-to-background dilution due to overlap of nearby Zeeman components, and angular factors $\tan\theta$, and $\cot\theta$. The result may be expressed as an effective systematic correction to each of the entries $\bar{\Delta}$ in Table III. Note that the E dependence of this correction is negligible. The corrected asymmetry Δ^* is plotted versus E^{-1} in Fig. 9(a). The data clearly reveal the E^{-1} dependence expected from PNC.

A straight line is fit to the weighted points of Fig. 9(a) by least squares. The effective systematic correction determines the constraint $\Delta^*(E=\infty)=(0\pm 10)\times 10^{-7}$. From the slope of the line we obtain

$$\text{Im}\frac{\mathscr{E}_P}{\beta}=(-1.73\pm 0.26\pm 0.07)\ \text{mV/cm}\ .\tag{58}$$

Here the first uncertainty is statistical and includes the uncertainty in (57). The second uncertainty in (58) is systematic and includes the uncertainties in $|E_{0y}|$ and $(\Delta E_x^{(1)}-\Delta E_x^{(2)})/E_{0y}$.

In Fig. 9(b) we plot the asymmetry for each Zeeman component separately, where we have combined the data or all four electric field values together by assuming a $1/E$ dependence, after correcting for finite signal-to-background. As expected, the two asymmetries have opposite sign and the relative magnitudes are consistent with a calculation of the asymmetry as a function of frequency [see Fig. 4(b)].

V. CONCLUSIONS

The present experimental result (58) is consistent with our earlier measurements of PNC in the 293-nm transition,[6] where the result

$$\text{Im}\frac{\mathscr{E}_P}{\beta}=-1.80^{+0.65}_{-0.60}\ \text{mV/cm}\tag{59}$$

was obtained. The present result (58) represents a major improvement because of the smaller overall uncertainty, and also because systematic corrections are now much smaller.

The goal is to determine the weak charge Q_W. For this purpose, we recall the two theoretical values of $\mathscr{E}_P$ presented in Sec. I.

$$\mathscr{E}_{P,\text{theor}}^{\text{OECF}}=(1.93\pm 0.40)\times 10^{-10}iQ_W\mu_0\ ,\tag{60}$$

$$\mathscr{E}_{P,\text{theor}}^{\text{RMBPT}}=(1.51\pm 0.07)\times 10^{-10}iQ_W\mu_0\ .\tag{61}$$

As mentioned earlier, the OECF value (60) results from a central field calculation (10) that ignores many-body effects (is of zeroth order in the electron-electron interaction). The RMBPT calculation (61) by Das and co-

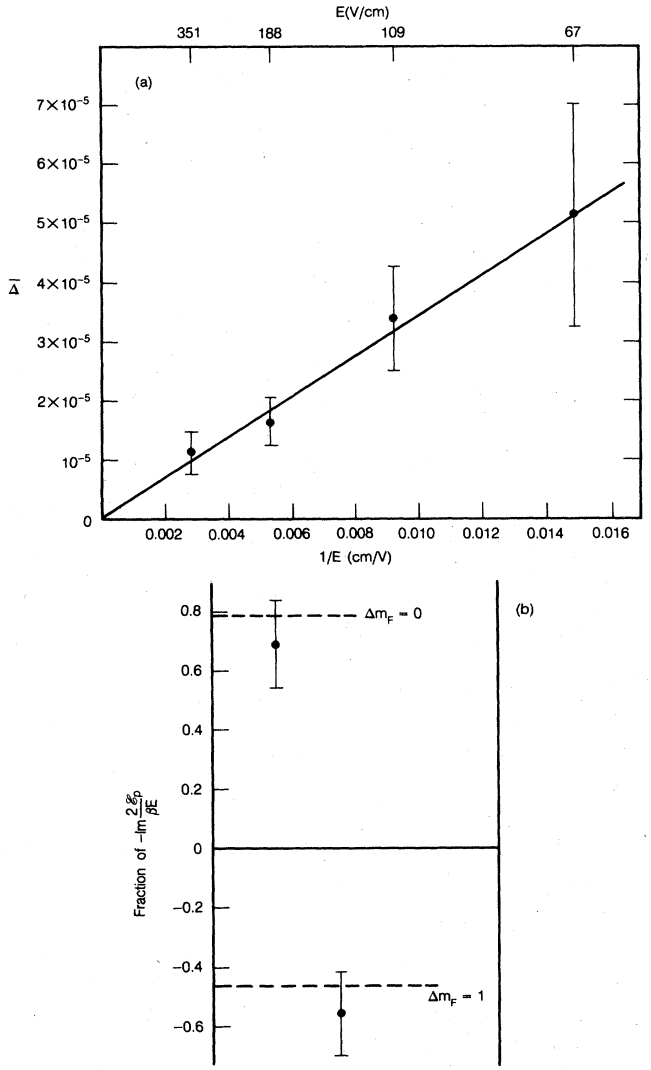

FIG. 9. (a) PNC asymmetry Δ^* averaged over the two Zeeman components vs $1/E$. The straight line is a least-squares fit to the data points (see text) and is not constrained to pass through the origin. (b) Experimental asymmetry, Δ for the two hyperfine components separately. The measured PNC asymmetries for the different values of electric field have been combined assuming a $1/E$ dependence. We plot the fraction of $-\mathrm{Im}2\mathscr{E}_P/\beta E$ measured on each transition. Dashed lines indicate the theoretical prediction for relative sizes of the asymmetry.

workers[11] obtains a zeroth-order result in good agreement with (60) but also takes into account first-order corrections. We therefore employ the RMBPT value (61) in the ensuing discussion.

To compare $\mathscr{E}_{P,\mathrm{theor}}$ with $(\mathrm{Im}\mathscr{E}_P/\beta)|_{\mathrm{expt}}$ in order to derive an empirical value of Q_W, one must know the value of β. Unfortunately, β is not yet known directly from experiment, (although we are at present carrying out such a measurement), nor was a theoretical value of β reported by Das and co-workers. Thus for the present we must rely on the OECF value[10] of β_{theor} given by Eq. (10). Dividing (61) by (10) and comparing with (57) we obtain

$$Q_W(^{205}_{81}\mathrm{Tl}) = -188 \pm 47 \ . \tag{62}$$

The uncertainty in (62) arises from the combination, in quadrature, of the uncertainty in $(\mathrm{Im}\mathscr{E}_P)/\beta|_{\mathrm{expt}}$, (19%), that in $\beta^{\mathrm{OECF}}_{\mathrm{theor}}$, (15%), and that in $\mathscr{E}^{\mathrm{RMBPT}}_{P,\mathrm{theor}}$, (5%). According to the standard SU(2)×U(1) electroweak model, $Q_W = Z(1-4\sin^2\theta_W) - N$. Inserting $Z=81$, $N=124$, and $\sin^2\theta_W = 0.215$ we have

$$Q^{\mathrm{Std}}_W(^{205}_{81}\mathrm{Tl}) = -113 \ . \tag{63}$$

Finally, comparing (62) and (63) we obtain

$$\Delta Q = Q_W - Q^{\mathrm{Std}}_W = -75 \pm 47 \ . \tag{64}$$

One can speculate on alternatives to the standard model[15] that would lead to $\Delta Q \neq 0$. For ^{205}Tl, we believe that such speculations are premature and must remain so until β is accurately measured and the RMBPT calculation is thoroughly checked.

ACKNOWLEDGMENTS

It is a pleasure to thank Steven Chu for his invaluable contributions to the laser system. This work was supported in part by the National Science Foundation and in part by a Bell Telephone Laboratories grant through the Graduate Research Program for Women. This research was supported by the Director, Office of Energy Research, Office of Basic Energy Sciences, Chemical Sciences Division of the U.S. Department of Energy under Contract No. DE-AC03-76SF00098.

*Present address: Physics Division, Lawrence Berkeley Laboratory, University of California, Berkeley, CA 94720.

[1]M. A. Bouchiat and C. Bouchiat, Phys. Lett. **48B**, 111 (1974); J. Phys. (Paris) **35**, 899 (1974); **36**, 493 (1975).

[2]T. P. Emmons, J. M. Reeves, and E. N. Fortson, Phys. Rev. Lett. **51**, 2089 (1983).

[3]H. Hollister *et al.*, Phys. Rev. Lett. **46**, 643 (1981), and references therein.

[4]C. Bouchiat, C. A. Piketty, and D. Pignon, Nucl. Phys. **B221**, 68 (1983).

[5]M. A. Bouchiat, J. Guena, L. Hunter, and L. Pottier, Phys. Lett. **117B**, 358 (1982); **134B**, 463 (1984).

[6]P. H. Bucksbaum, E. D. Commins, and L. R. Hunter, Phys. Rev. D **24**, 1134 (1981).

[7]This method was proposed independently by M. A. Bouchiat, M. Poirier, and C. Bouchiat, J. Phys. (Paris) **40**, 1127 (1979); and by E. Commins [see P. H. Bucksbaum, in Proceedings of the Workshop on Parity Violation in Atoms, Cargese, Corsica, 1979 (unpublished)].

[8]P. S. Drell and E. D. Commins Phys. Rev. Lett. **53**, 968 (1984).

[9]S. Chu, E. D. Commins, and R. Conti, Phys. Rev. Lett. A **60**, 96 (1977).

[10]D. Neuffer and E. D. Commins, Phys. Rev. A **16**, 844 (1977).
[11]B. P. Das *et al.*, Phys. Rev. Lett. **49**, 32 (1982).
[12]P. S. Drell and S. Chu, Opt. Commun. **28**, 343 (1979).
[13]M. Kasha, J. Opt. Soc. Am. **38**, 929 (1948).
[14]A. Flusberg, T. Mossberg, and S. R. Hartmann, Phys. Rev. A **14**, 2146 (1976).
[15]C. Bouchiat and C. A. Piketty, Phys. Lett. **128B**, 73 (1983).